**ROYAL SOCIETY OF CHEMISTRY**

## PAPER

Check for updates

# Synthesis of micro- and nanosheets of CrCl₃–RuCl₃ solid solution by chemical vapour transport†

Samuel Froeschke, [ID] *[a] Daniel Wolf,[a] Martin Hantusch,[a] Lars Giebeler, [ID] [a] Martin Wels,[b] Nico Gräßler, [ID] [a] Bernd Büchner,[a,c] Peer Schmidt [ID] [b] and Silke Hampel [ID] [a]

Solid solutions of 2D transition metal trihalides are rapidly growing in interest for the search for new 2D materials with novel properties at nanoscale dimensions. In this regard, we present a synthesis method for the $Cr_{1-x}Ru_xCl_3$ solid solution and describe the behaviour of the unit cell parameters over the whole composition range, which in general follows Vegard's law in the range of $a = 5.958(6)_{CrCl_3} \ldots 5.9731(5)_{RuCl_3}$ Å, $b = 10.3328(20)_{CrCl_3} \ldots 10.34606(21)_{RuCl_3}$ Å, $c = 6.110(5)_{CrCl_3} \ldots 6.0385(5)_{RuCl_3}$ Å and $\beta = 108.522(15)_{CrCl_3} \ldots 108.8314(14)_{RuCl_3}$ °. The synthesized solid solution powder was subsequently used to deposit micro- and nanosheets directly on a substrate by applying chemical vapour transport in a temperature gradient of 575 °C → 525 °C for 2 h and 650 °C → 600 °C for 0.5 h as a bottom-up approach without the need for an external transport agent. The observed chromium chloride enrichment of the deposited crystals is predicted by thermodynamic simulation. The results allow for a nanostructure synthesis of this solid solution with a predictable composition down to about 30 nm in height and lateral size of several μm. When applying a quick consecutive delamination step, it is possible to obtain few- and monolayer structures, which could be used for further studies of downscaling effects for the CrCl₃–RuCl₃ solid solution. X-ray photoelectron spectroscopy, transmission electron microscopy and Raman spectroscopy were used to confirm the purity and quality of the synthesized crystals.

## Introduction

Ever since the discovery of the unthought properties of graphene and other 2D materials that arise from the downscaling of their bulk crystal structure down to nanometre dimensions, the search for new materials with 2D crystal structure and interesting properties did not slow down. Since then many such 2D materials were rediscovered for various applications, such as $MoS_2$,[1] $hBN$[2] or phosphorene,[3] and countless more. The material class of transition metal trihalides $MX_3$ (TMTH) also hosts several compounds with a 2D crystal structure that, in their most common modifications with $BiI_3$ and $RhBr_3$ structure types, are very similar to each other.[4] This isostructural property enables the formation of solid solutions, with which it is possible to create new 2D materials with modified or even completely new properties.

The TMTHs $CrCl_3$ and $RuCl_3$ were already intensely studied because of their unusual magnetic properties,[5,6] whereas $RuCl_3$ is most famous as a possible Kitaev spin liquid candidate.[7] Their solid solution has been known for several years[8] and has received more attention recently because of the described possibilities for the formation of mixed crystals, especially related to the magnetic properties of Cr-doped $RuCl_3$ crystals.[9,10] The solid solution crystallises in the entire composition range in the space group $C2/m$ ($RhBr_3$ structure type), isostructural to the parent compounds. The cation sites in the crystal structure are randomly occupied by $Cr^{3+}$ and $Ru^{3+}$.[8]

Besides the very interesting magnetic and optical[11] properties of the bulk solid solution material, which for example features a spin liquid state for intermediate Cr : Ru ratios,[9] one could expect that the properties of the solid solution will change when the height of the crystalline material is scaled from bulk dimensions, over micro- and nanometre heights down to only few- or even monolayer structures, since such exotic behaviour is known for pure $CrCl_3$[12,13] and $RuCl_3$.[14,15] The investigation of these expectable changes during the downscaling could provide crucial insights on the tuneability of nanomaterial properties by solid solution formation. For detailed and complex investigation of such nanoscale material

*[a]Leibniz Institute for Solid State and Materials Research Dresden, 01069 Dresden, Germany. E-mail: s.froeschke@ifw-dresden.de*
*[b]Brandenburg University of Technology Cottbus-Senftenberg, 01968 Senftenberg, Germany*
*[c]Technische Universität Dresden, 01069 Dresden, Germany*
†Electronic supplementary information (ESI) available. See DOI: https://doi.org/10.1039/d2nr01366e

properties, high-quality micro- and nanostructures of the respective material are required, about which to our best knowledge no designated studies were published yet. The synthesis of such nanostructures could be realized by a conventional top-down approach such as exfoliation of bulk crystals. However, a bottom-up approach can have many advantages like crystals with distinct shapes and edges or a deposition directly on a substrate.

In this study we therefore investigate the synthesis of such nanostructures of $Cr_{1-x}Ru_xCl_3$. A scheme of the experimental procedure is shown in Fig. 1. For the deposition of nanocrystals, we chose chemical vapour transport (CVT) without addition of an external transport agent. By optimising the transport parameters with the help of theoretical calculations and transport process simulations, we find experimental parameters to deposit the desired nanostructures, like it has been shown in previous studies with a similar approach.[16–18] Since other studies observed the enrichment of a certain element during the CVT of mixed compounds,[19,20] we additionally investigate enrichment processes during the CVT of $Cr_{1-x}Ru_xCl_3$ that have not been described in literature yet. For this purpose, we combine quasi-stationary transport conditions with short transport durations and homogeneous, presynthesized starting material to ensure stable and consistent transport conditions.

We also present a method to easily delaminate the as-grown nanocrystal to potentially obtain few- and even monolayer structures directly on the substrate without the need for exfoliation. In the future, these structures could be used for further characterisation, e.g. regarding downscaling effects.
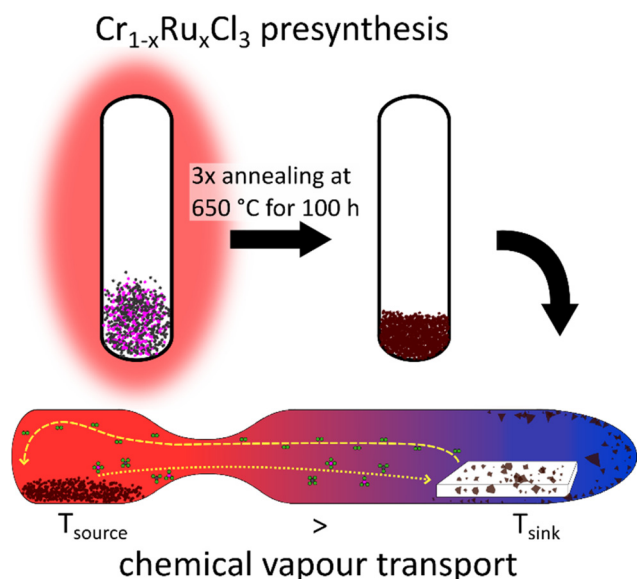


**Fig. 1** Schematic illustration of the synthesis processes. Homogeneous solid solution powder is synthesized by repeated tempering of $CrCl_3$ and $RuCl_3$. This is then used as starting material for CVT experiments to deposit nanocrystals directly on a substrate.

# Experimental

## Purification of starting materials ($CrCl_3$, $RuCl_3$)

Commercial powders of $CrCl_3$ (99.9% metal basis, Alfa Aesar) and $RuCl_3$ (45–55% Ru content, Aldrich Chemistry) were purified by initial treatment via CVT before use in all synthesis experiments due to the significant contaminations of commercial $CrCl_3$ and $RuCl_3$ with varying amounts of water and oxygen (see ESI S1†). Several grams of $CrCl_3$ were transported from 800 °C → 700 °C for a few days, whereas oxygen contaminations remain separated in the source in the form of green $Cr_2O_3$ powder. Pure $RuCl_3$ was obtained by transporting 1 g commercial $RuCl_3$ powder from 800 °C → 700 °C for around 40 h. During the transport significant amounts of chlorine are released which still remain gaseous after cooling to room temperature. Hence the source of the ampoule was cooled with liquid nitrogen to condense the chlorine vapour inside completely before opening the ampoule and storing the purified $RuCl_3$ under inert atmosphere. For sufficient purification the transport must be stopped before the $RuCl_3$ in the source is depleted and a sequential transport of $RuO_2$ starts. For additional information about the CVT see ESI S1.†

## Synthesis of $Cr_{1-x}Ru_xCl_3$ powder

Purified $CrCl_3$ and $RuCl_3$ were weighted in (2.5 mmol in total) at the desired ratio and mixed in an agate mortar under argon atmosphere. After the powder was filled into a fused silica ampoule, the ampoule was sealed at a pressure of approximately $3 \times 10^{-3}$ mbar and tempered for 100 h in a muffle furnace. The furnace was then cooled to 400 °C with 1 K min$^{-1}$ before naturally cooling down to room temperature. To ensure a complete formation of a homogeneous solid solution, the obtained powder was grinded again and the procedure was repeated for 2 times (3 heat treatments in total).

## Preparation of substrates

Substrates with dimensions of $10 \times 10 \times 0.5$ mm$^3$ of yttria-stabilised zirconia (9.5 mol% $Y_2O_3$, Crystal GmbH) with the (111) surface side polished (YSZ (111)) were spin-coated with photoresist on the polished side and then cut into 6 equal pieces of $5.0 \times 3.3 \times 0.5$ mm$^3$. These substrates were then cleaned by removing the photoresist with acetone and consecutive cleaning steps by ultrasonication in acetone, isopropanol and distilled water for 15 min each. After the last ultrasonic treatment, the substrates were rinsed with distilled water and remaining water was removed with pressurised nitrogen.

## Growth of micro- and nanocrystals on substrates

In a glovebox 4 to 10 mg of grinded solid solution powder were filled into the source area of a two-chamber fused silica (ilmasil PN, qsil, max. 45 ppm OH content) ampoule (12 cm long, 1 cm diameter, 0.5 cm narrowing diameter) and a YSZ (111) substrate was placed in the sink with the polished side facing up. The distance between the source material and the substrate was 10 cm in all experiments. The ampoule was then sealed outside the glovebox at a pressure of $3 \times 10^{-3}$ mbar and

placed into a two-zone furnace (LOBA, HTM Reetz GmbH). CVT was performed by heating both zones with a rate of 10 K min⁻¹ to the target temperatures, holding these temperatures for the desired time, then taking the ampoule out of the furnace and quenching it with water. Most experiments were performed with a temperature gradient of 575 °C → 525 °C for 2 h and 650 °C → 600 °C for 0.5 h (time started when source reached target temperature).

### Delamination of nanocrystals on substrates

To remove excess crystals and obtain few layer structures, the substrate was placed in 2 mL of $N$-methyl-2-pyrrolidone (NMP, VWR) inside a small glass vessel, ultrasonicated for 1 to 3 min, taken out of the solvent and the excess solvent was removed with pressurised nitrogen.

### Characterisation techniques

Powder X-ray diffraction (pXRD) was performed with Co-K$_\alpha$ radiation in reflection geometry ($\lambda_{K\alpha1}$ = 1.78901 Å, $\lambda_{K\alpha2}$ = 1.79290 Å, PANalytical X'Pert Pro, X'Celerator detector, 0.01° step size) as well as in transmission geometry ($\lambda$ = 1.78896 Å, STOE STADI-P, Ge (111) primary beam monochromator, Mythen 1K detector, 0.015° step size), both with a few mg of Si powder (99.5%, −325 mesh, Alfa Aesar, LOT: R30D007) added as an internal standard. The refinement of the unit cell parameters and their estimated standard deviation was conducted with the software "GSAS-II" version 5190,[21] sample offsets were calculated with reference to the internal Si-standard ($a$ = 5.429112(26) Å, value refined in relation to NIST 640d standard). Starting parameters for the refinement were taken from literature values for CrCl$_3$[22] and RuCl$_3$,[23] whereas atomic coordinates and Wyckoff positions of the solid solutions were estimated to be the same as in CrCl$_3$. Starting parameters for the solid solutions were derived from Vegard's law.

Light microscopy imaging was performed with AXIO Imager A1 m (Zeiss).

Solid solution powder and substrates were investigated by scanning electron microscopy (SEM) with a "FEI Nova NanoSEM 200" (FEI company) with an Everhart–Thornley detector for regular pictures and a backscattering electron detector for element contrast pictures. 5 kV were used as acceleration voltage. Prior to the analysis by SEM or energy dispersive X-ray spectroscopy (EDX), the samples were stuck on a conducting carbon tape and sputtered with about 90 nm carbon film using the Carboncoater EMITECH K450 (Emitech group) and a twisted carbon yarn with 1 mm in diameter and 0.7 g m⁻¹ (PLANO GmbH).

In combination with the SEM device, EDX was performed with a QUANTA 200/400 (AMATEX) with 50 s measurement time and 15 kV acceleration voltage. Quantification was performed with the software "Genesis Spectrum" version 6.32. To increase the precision of the EDX quantification results, a calibration was used (for details see ESI S2†).

Simultaneous thermal analysis (STA) was performed with a "STA 449 F3 Jupiter" (NETZSCH-Gerätebau GmbH). 10 mg sample were placed in an Al$_2$O$_3$ crucible (85 µL) with pierced

lid, while measurements were performed with 10 K min⁻¹ heating rate from 40 °C to 1080 °C with Ar (Premium 5.2, Air Products) gas flow of 70 mL min⁻¹.

The heights of nano- and microcrystals were measured with an "Dimension icon" atomic force microscope (AFM, Bruker) in tapping mode with a Si single crystal as cantilever, a scan rate of 0.3 Hz, a line length between 2 and 40 µm depending on the size of the structure and 1024 samples per line. The software "Nanoscope Analysis" version 1.8 was used for data analysis. The substrate surface was used for background fitting.

Micro-Raman measurements were performed with a T64000 Spectrometer (Horiba Jobin Yvon, USA) using a 532 nm laser excitation from a Torus 532 Laser (Laser Quantum).

For the preparation of transmission electron microscopy (TEM), as-grown substrates were ultrasonicated in 500 µL NMP for 3 min. A tiny portion of the fresh dispersion was pipetted onto lacey-carbon copper grids (Science Services GmbH, 200 mesh) and air-dried. This procedure was repeated 3 times with the same grid. Aberration-corrected high resolution TEM imaging was performed using a FEI Titan3 80–300 microscope (Thermo-Fisher Company) at 300 kV acceleration voltage. Electron diffraction studies were conducted to determine the crystal structure over a region of a few micrometres. The diffraction patterns were indexed with the help of the Single-Crystal software package (CrystalMaker Software Ltd, UK).

X-ray photoelectron spectroscopy was performed with a "PHI 5600" (Physical Electronics) spectrometer using monochromatic Al-Kα radiation (200 W) and equipped with a hemispherical analyser with 29.35 eV pass energy for high resolution spectra. The estimated spot size on the sample is approximately 0.4 mm. To avoid charging effects, an electron gun as neutraliser is used during each measurement. All binding energies are referenced to the C 1s peak at 284.8 eV.

### Thermodynamic simulations

For thermodynamic calculations and CVT simulations a modified version of the software package "TRAGMIN 5.1"[24] was utilized. A volume of 9.4 mL with 0.04 mmol starting substance, $5 \times 10^{-9}$ mol H$_2$O traces and $1 \times 10^{-9}$ mol argon traces were specified for the simulation. The used thermodynamic data and additional details about the simulations can be found in the ESI S3.†

## Results and discussion

In order to establish reproduceable starting conditions for the desired experiments on the nanocrystal deposition by chemical vapour transport, it is necessary to provide pure and homogeneous solid solution starting material with a known composition. For this reason, we prepared powder samples of the solid solution at 10 mol% intervals over the entire composition range.

### Structural analysis of Cr$_{1-x}$Ru$_x$Cl$_3$ powder

The structural properties and the purity of the synthesized mixed compound samples were confirmed by pXRD. As

described by Roslova *et al.* the diffraction patterns show strong texture effects when measured in Bragg–Brentano geometry (reflection), which can cause significant errors for the determination of the unit cell parameters.[25] To overcome this issue and to further increase the precision, pXRD was carried out with Co radiation in both reflection as well as in transmission geometry. When measuring in transmission geometry, the texture inverts, allowing for an observation of different reflections than in the reflection measurements. A comparison between the observed reflections for reflection and transmission measurements is shown in Fig. 2, whereas the data are background subtracted and normalized for overview reasons. For an overview of the unmanipulated data, see ESI Fig. S4 and S5.†

For all samples, no reflections of impurities such as $Cr_2O_3$, Ru or $CrCl_2$ as well as no reflection splitting was observed, confirming the purity of the samples and a complete formation of homogeneous solid solution. When following the evolution of the reflections in Fig. 2, all reflections of the mixed samples can be assigned to originate from pure $CrCl_3$ and/or $RuCl_3$, thus confirming that the crystal structure and space group remain intact over the hole course of the solid solution. With this confirmed, the crystal structure of the solid solution can be discussed similar to those of $CrCl_3$ and $RuCl_3$, see Fig. 3. Most importantly, the lattice parameters $a$ and $b$ define the lattice inside the 2D layer, while $c$ and $\beta$ describe the stacking of the respective layers, applying the monoclinic space group $C2/m$. The cation sites form a hexagonal arrangement while being octahedrally coordinated by the Cl. Each neighbouring stacked layer is shifted in direction of the $a$-axis for $\frac{1}{4}a$, resulting in an ABC stacking sequence.

Observed reflection broadening in the diffraction pattern, for example at around 21 and 41°, is the result of diffuse scattering due to stacking faults, which is commonly observed for all kinds of 2D materials. By combining reflection and transmission patterns, we performed a refinement of the unit cell parameters for all samples. For the refined results of the unit cell parameters, see ESI Table S3.† Our results were compared with literature values of Roslova *et al.* and are depicted in Fig. 4. In contrast to their reported data, our measurements show a uniform trend for all parameters. Taking the common underestimation of the refinement error into account, our results agree with Vegard's law and suggest an ideal mixing behaviour between $CrCl_3$ and $RuCl_3$. Because of the monoclinic unit cell, the hexagonal arrangement of cations in the (001) planes is not ensured by symmetry relations and in theory also allows the description of distorted arrangements like in $MoCl_3$.[26] To check, if the hexagonal arrangement is dis-
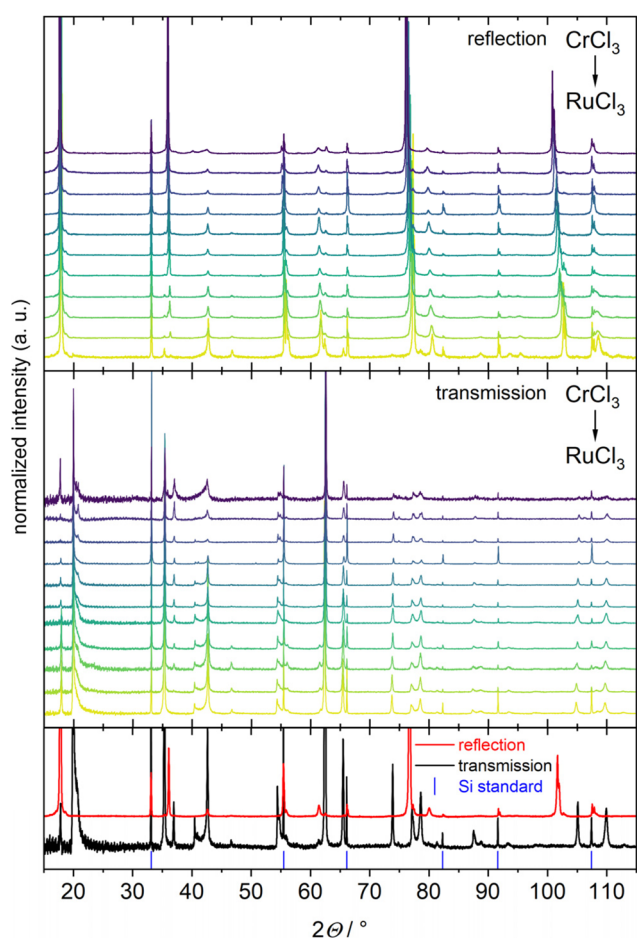


**Fig. 2** Normalized, background subtracted and stacked powder XRD pattern of the $Cr_{1-x}Ru_xCl_3$ solid solution series in steps of 10 mol%, measured in (a) reflection and (b) transmission geometry. (c) Comparison of observable peaks between reflection (red) and transmission (black) geometry for the same $x = 0.5$ sample.
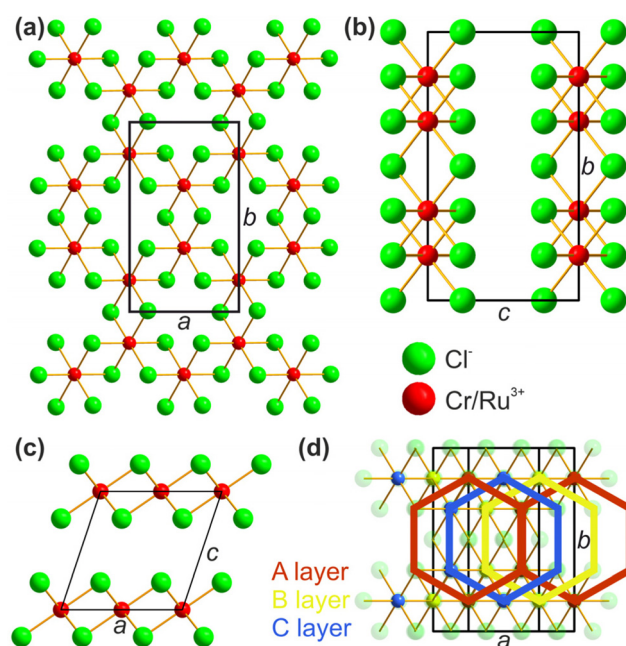


**Fig. 3** Crystal structure of $CrCl_3$ and $RuCl_3$: (a) view onto a single [001] plane, (b) side view along the $a$-axis, (c) side view along the $b$-axis, (d) top view upon multiple [001] planes with highlighted stacking direction along the $a$-axis.
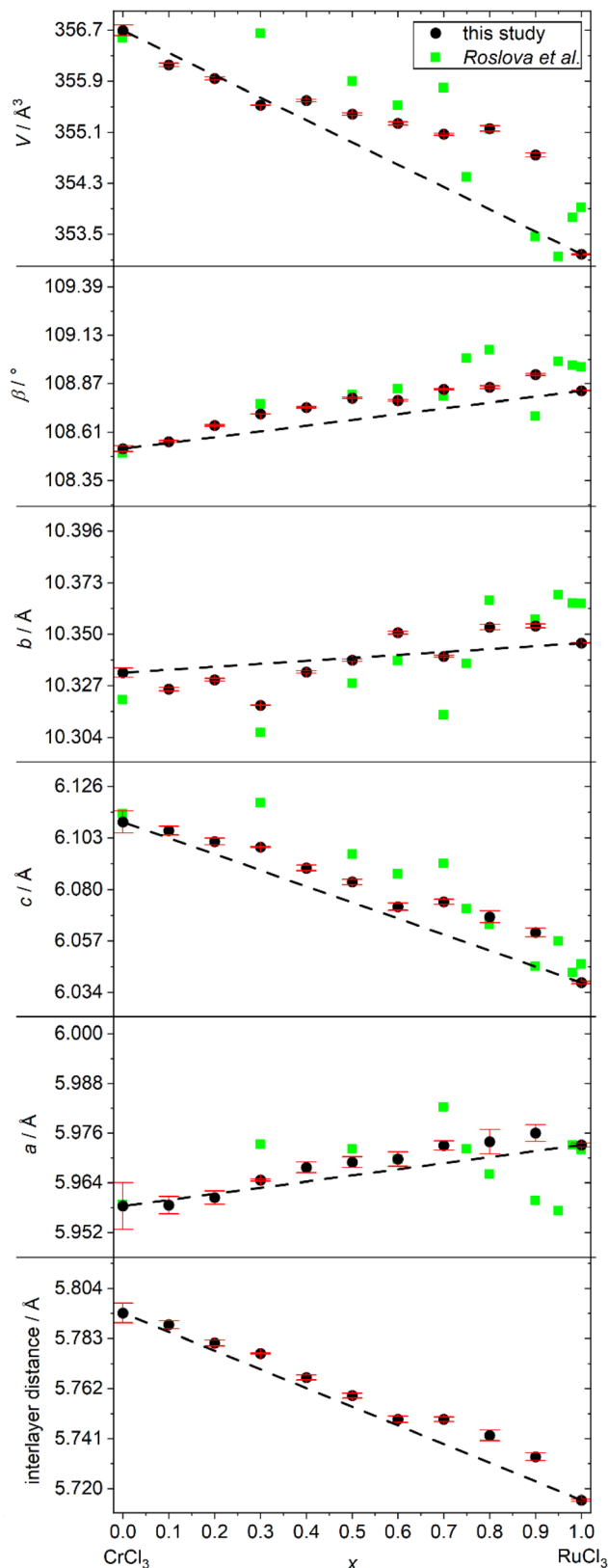
**Fig. 4** Refined unit cell parameters of $Cr_{1-x}Ru_xCl_3$ compared to values of Roslova *et al.*[25] and Vegard's law. Error bars are estimated standard deviations derived from the refinement software.
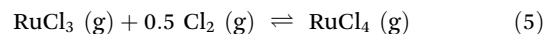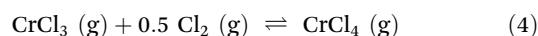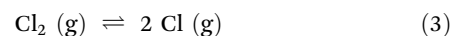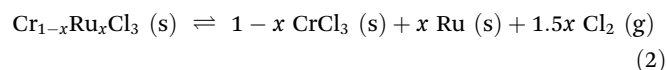
torted or not, one can compare the length of the *a*- and *b*-axis, since for a perfect undistorted hexagonal arrangement the following axes must meet the following equation:

$$a \cdot \sqrt{3} = b$$

The calculated values for the series of mixtures can be found in ESI Table S3† and are all equal to 1 within the expectable range of errors, also hinting towards an ideal solid solution with undistorted hexagonal arrangement of the cations.

## Thermodynamic calculations and CVT simulation

To predict the complex chemical behaviour and estimate suitable parameters for the desired growth of $Cr_{1-x}Ru_xCl_3$ nanocrystals by chemical vapour transport, we calculated the chemical equilibria during the vapour phase transport process. Fig. 5(a) displays the calculated partial pressures of the vapour species over a composition with $x = 0.5$. Since only vapour species with a partial pressure higher than approximately $10^{-6}$ to $10^{-5}$ bar can contribute in a recognizable way to vapour transport processes,[27] only a few species have direct influence on the transport process in this system (when there are only traces of oxygen present and no external transport agent is added). $CrCl_3$ (g) and $CrCl_4$ (g) are the most stable and therefore relevant species regarding the transport of chromium and $RuCl_3$ (g) and $RuCl_4$ (g) for ruthenium. In accordance with Grönke *et al.*,[28,29] we obtain the following transport relevant chemical equilibria that are responsible for the CVT from the calculated transport efficiencies (see ESI S2†):

$$Cr_{1-x}Ru_xCl_3 \ (s) \ \rightleftharpoons \ 1 - x \ CrCl_3 \ (g) + x \ RuCl_3 \ (g) \quad (1)$$

$$Cr_{1-x}Ru_xCl_3 \ (s) \ \rightleftharpoons \ 1 - x \ CrCl_3 \ (s) + x \ Ru \ (s) + 1.5x \ Cl_2 \ (g) \quad (2)$$

$$Cl_2 \ (g) \ \rightleftharpoons \ 2 \ Cl \ (g) \quad (3)$$

$$CrCl_3 \ (g) + 0.5 \ Cl_2 \ (g) \ \rightleftharpoons \ CrCl_4 \ (g) \quad (4)$$

$$RuCl_3 \ (g) + 0.5 \ Cl_2 \ (g) \ \rightleftharpoons \ RuCl_4 \ (g) \quad (5)$$

With respect to reactions (4) and (5) the total amount of $CrCl_4$ (g) and $RuCl_4$ (g) depends on the amount of chlorine vapour in the system. When performing a CVT of this solid solution without the addition of chlorine as an external transport agent, the amount of chlorine is essentially determined by the decomposition described by reaction (2). The $MCl_3$ (g) : $MCl_4$ (g)-ratios are therefore depending on the amount of released chlorine due to the decomposition to elemental ruthenium in reaction (2).

With respect to the calculated partial pressures, a transport of ruthenium by $RuCl_3$ (g) or $RuCl_4$ (g) should only be possible for temperatures higher than 500 °C. To partially compare the thermodynamic behaviour predicted by simulations with experimental data, comparative STA measurements were performed on an $x = 0.5$ sample. Further details and the underlying data can be found in ESI S3.† Although the STA measurements were performed in the open system and reflect the con-
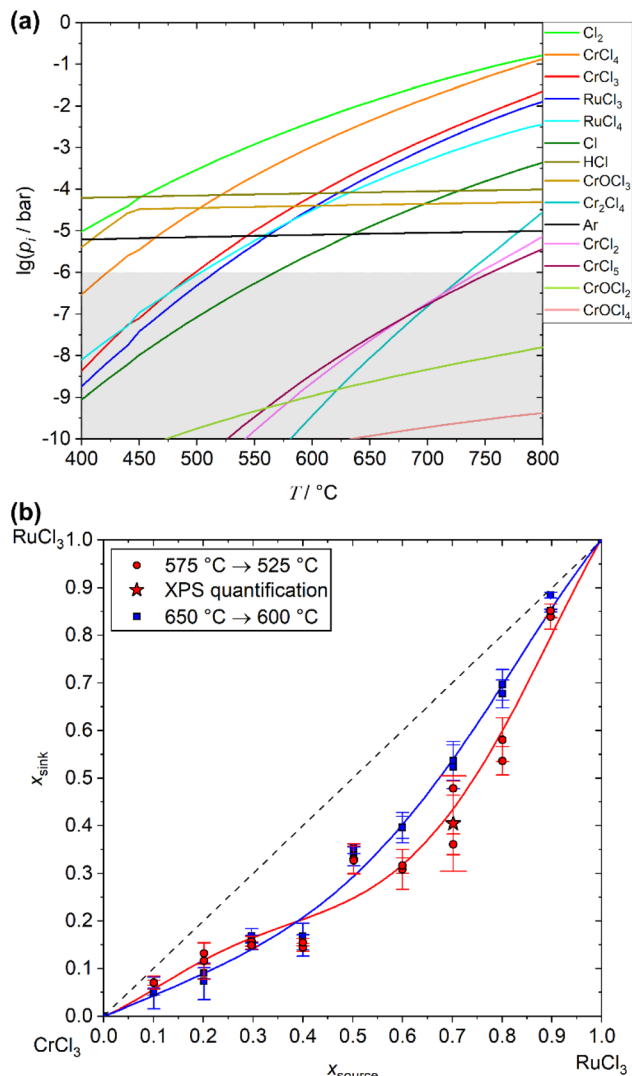
**(a)**



**(b)**



Fig. 5  (a) Calculated partial pressures of known vapour species over a $Cr_{1-x}Ru_xCl_3$ sample with $x = 0.5$ including traces of $H_2O$ and Ar. The grey area indicates pressures that are too low for transport relevance. (b) Observed values of $x$ of deposited crystals in the sink. Solid lines are only added to guide the eye. Error for EDX measurements is the standard deviation. Error for XPS measurement estimated with 0.1.

ent is too low, no supersaturation on the surface of the substrate will occur, thus the formation of seeds is prevented which is usually necessary to start the crystal growth process. Keeping this in mind, a transport from 575 °C → 525 °C should result in relatively low transport rates, but simultaneously might allow seed formation on the substrate.

The calculated partial pressures of the relevant vapour species show higher concentrations of chromium species in the vapour phase compared to the ruthenium species concentrations. In combination with their temperature dependency, the simulations therefore predict an enrichment of chromium chloride for the deposition of the mixed crystals in the sink compared to the starting material in the source over the whole range of starting compositions. Such an enrichment in the sink unavoidably leads to a depletion of chromium in the source material, again changing partial pressures of the transport relevant vapour species and resulting in a composition change of the deposited material in the sink. When such a time dependent transport will be performed for a long duration, *e.g.* for the growth of bulk crystals, this predicted enrichment might result in crystals with a composition gradient along the growth direction, when the diffusion of cations inside the crystal might not be able to balance this gradient.

This predicted enrichment during the CVT of the solid solution was investigated by performing the transport only for a short duration, so that only small amounts of material, compared to the total amount in the source, was transported and no significant enrichment of the starting material occurs (quasi-stationary transport conditions).

### Deposition of crystals on the substrate

Systematic short duration transport experiments were performed at two different temperature gradients (575 °C → 525 °C for 2 h and 650 °C → 600 °C for 0.5 h) to screen the predicted enrichment of chromium chloride for the deposited mixed crystals in the sink during the transport. The obtained values of $x$ of the crystals grown on top of the substrate are shown in Fig. 5(b), for detailed values see ESI Table S4.† The experimental results confirm the enrichment of chromium chloride during the transport process which was predicted by the simulation. Comparing the values for the investigated temperatures, the enrichment effect is stronger at the lower mean temperature for $x > 0.5$ (Ru-rich starting material), while it seems to be about equal for $0 < x < 0.5$ (Cr-rich starting material). This enrichment of the chromium content must be considered when growing $Cr_{1-x}Ru_xCl_3$ bulk- or nanocrystals by chemical vapour transport. Deposited crystals on the same substrate showed only small deviations in their composition. The deposited nanocrystals itself exhibit a homogeneous distribution of the respective elements without any signs of phase- or concentration separations, as confirmed by EDX mapping (see ESI Fig. S6†). For experiments with the same starting material, the deviation of the measured composition of the deposited crystals is smaller than 10%. Both deviations might be caused by errors of EDX as a method, but also by slight differences in the experimental parameters and a slight

ditions of the closed-system calculations and CVT experiments only to a limited extent, the results show a very good agreement with the predicted temperatures. An endothermic signal starts to evolve at about 520 °C which is coupled to a starting decrease in mass that becomes increasingly stronger as the temperatures continues to rise. This observation can be attributed to the start of noticeable sublimation due to reaction (1) in combination with marginal decomposition of (2), which is in total agreement with the results of the simulation.

To achieve a growth of the desired nanocrystals with lateral dimensions in the μm-range, low transport rates and, thus, low temperatures are desired. The transport rate can also be controlled by the choice of the temperature gradient, whereas lower gradients result in lower transport rates. When the gradi-

deviation from quasi-stationary transport conditions. The results confirm that with the methodology presented here, the composition of the as-grown crystals can be reliably controlled, even directly on top of the substrate.

In addition to the investigation of enrichment processes during the CVT, the experimental parameters were optimised in a way to deposit micro- and nanocrystals of the solid solution with heights in the very low nm regime and lateral sizes of several μm. The best results for such growth were obtained for a temperature gradient from 575 °C → 525 °C with a transport duration between 30 min to 2 h, depending on the starting composition. Shorter durations were applied for Cr-rich starting materials, longer duration for Ru-rich ones based on the fact, that the transport rate increases with increasing amount of chromium. Even though a large portion of the deposited crystals is not epitaxially attached to the substrate surface or intergrown within agglomerates (see Fig. 6(a)), some of the crystals with heights >100 nm grow flat on the surface. The so obtainable nanocrystals show some but not completely distinct edges in most cases, like in Fig. 6(b). AFM measurements confirm a flat surface with some particles (see ESI Fig. S7†). Some crystals have partially elevated facets that are the result of additional layers growing on top. Typical nanocrystals show heights of about 30 to 70 nm and lateral dimensions between 2 and 20 μm.

When decreasing the mean temperature beneath 550 °C, the transport rate decreases significantly, yet the overall quality of the deposited crystals is suffering as well, resulting in crystals with less clean edges and less nanocrystals in total. The reason might be found in the reduced number of formed seeds on the substrate due to weaker supersaturation during the induction period of the vapour transport, thus decreasing the probability for the formation of nanocrystals.

When epitaxial deposited nanocrystals grow in height, they eventually become microcrystals, that are also observed for the experiments. In a height range of about 0.5 to 2 μm, these crystals show a strong light-refractive behaviour, as visible in Fig. 6(c). In this height range, even small steps change the light refractions as visible in the optical microscope. According to these observations, we conclude that the visible effect is most likely a result of thin film interference in combination with the optical properties of the material itself.

### Characterisation of nanocrystals

In order to investigate the quality and certain properties of the deposited nanocrystals, several characterisation techniques were applied. For this purpose, nanocrystals grown from starting material with a composition of $x = 0.7$ were used for the following investigations.

To confirm the high crystallinity and crystal structure of the deposited crystals, HRTEM investigation were performed. The representative results in Fig. 7(a) and (b) show a highly periodic arrangement of atoms inside the flakes. The Fourier transform of the high-resolution image of the nanoflakes oriented along [001] zone axis (Fig. 7(c)) shows very discrete reflections that are in excellent agreement with the simulated electron diffraction pattern obtained from the refined pXRD structure model for a composition of $x = 0.4$ (see ESI Fig. S8†). This is consistent with the enrichment results obtained from the EDX measurements, confirming the significant enrichment of chromium at the cation site during the transport experiments (Fig. 5(b)).

In order to investigate possible anomalies of the as-grown nanocrystals and to compare the results with literature reference, Raman measurements were performed on several crystals on the same substrate. In Fig. 8(a) representative measurement is compared with the theoretical peak positions for the parent compounds $CrCl_3$ and $RuCl_3$ taken from literature ref. 30 and 31. All observed peaks are explainable with a combination of modes from the parent compounds, which is consistent with the finding from Roslova et al.[25] Raman spectra taken from different crystals on the same substrate show no differences in peak positions (see ESI Fig. S9†), being an additional confirmation of the homogeneity of grown crystals on the substrate for the same experiment as well as for quasi-stationary transport conditions.
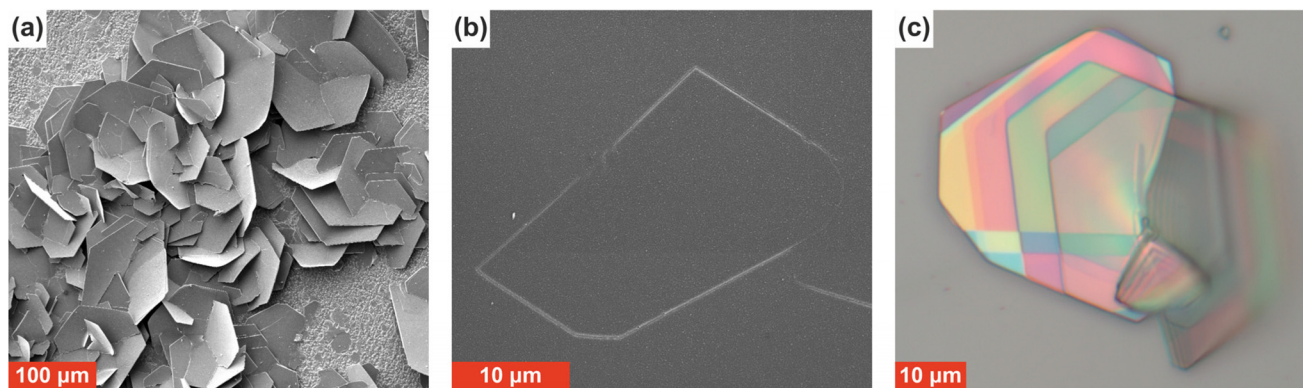


**Fig. 6** SEM image of (a) non-epitaxial grown crystal agglomerates and (b) a single as-grown nanosheet of about 30 nm in height (visible surface particles and cracks caused by carbon sputtering). (c) Microscope image of a microcrystal showing layer steps of a few nanometres distinguishable by colour.
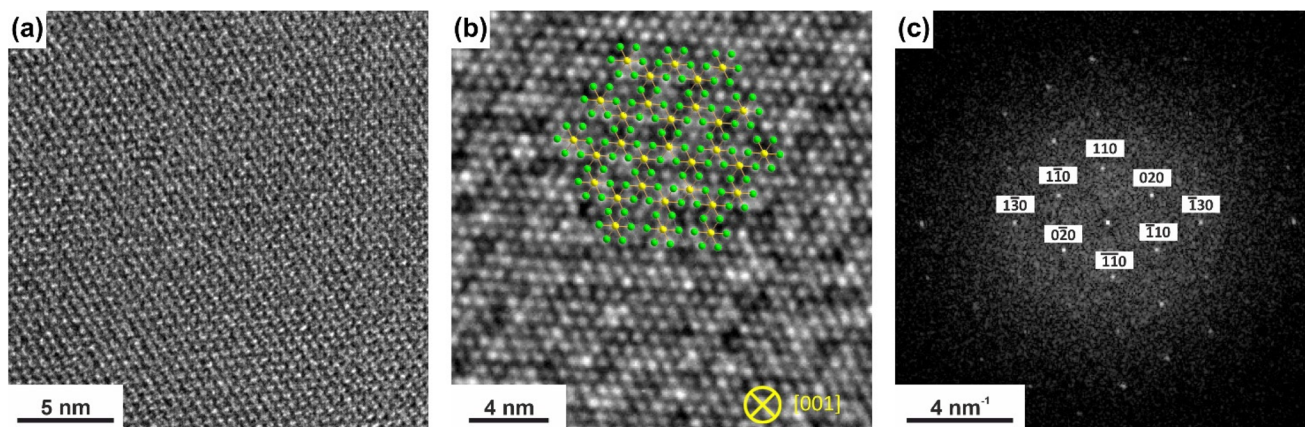
**Fig. 7** HRTEM investigations on as-grown $CrCl_3$–$RuCl_3$ nanoflakes: (a) HRTEM image recorded along [001] zone axis of the monoclinic lattice. (b) Image at higher magnification as (a) but at the same crystal orientation with overlaid atomic model (Ru/Cr − yellow, Cl − green). (c) Fourier transformed image (a) with some of the reflections indexed.
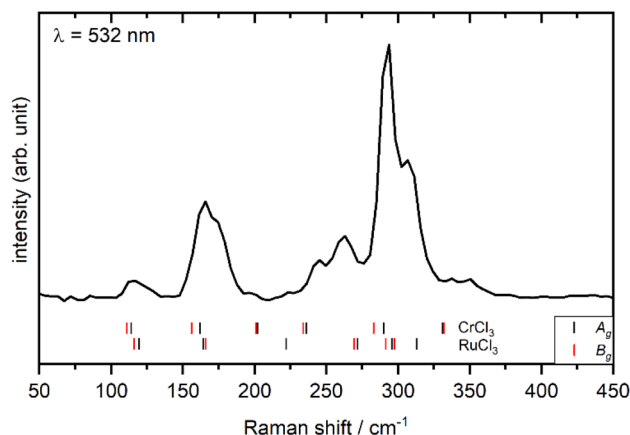


**Fig. 8** Raman spectrum of a nanocrystal with $x = 0.4$ compared to reference peaks for the parent compounds $CrCl_3$[26] and $RuCl_3$.[27]

XPS characterisation was also used to investigate the sample quality. The relevant element specific regions are shown in Fig. 9, for the overview spectrum, see ESI Fig. S10.† All measurements confirm the absence of surface oxidation or any other impurities of the solid solution crystals. The observed peaks for Cr 2p, Ru 3p, Cl 2s and Cl 2p do not show any signs of non-statistical occupation of the cation positions in the lattice and are all assigned to a single chemical environment of these elements. The Ru peak of highest intensity Ru 3d unfortunately overlaps with the C 1s peak, preventing it from use for quantification. The experimental quantification of the Cl : (Cr + Ru) ratio shows a higher ratio of 4.3 (using Cl 2s) than the expected value of 3.0. This deviation can be explained by low intensities in general and by taking the limited mean free path of about 2 nm into account. Calculating the more reliable Cr : Ru ratio from the XPS data gives a value of 1.47 which corresponds to an $x$-value of 0.4. This again is consistent with the EDX analysis of samples pro-
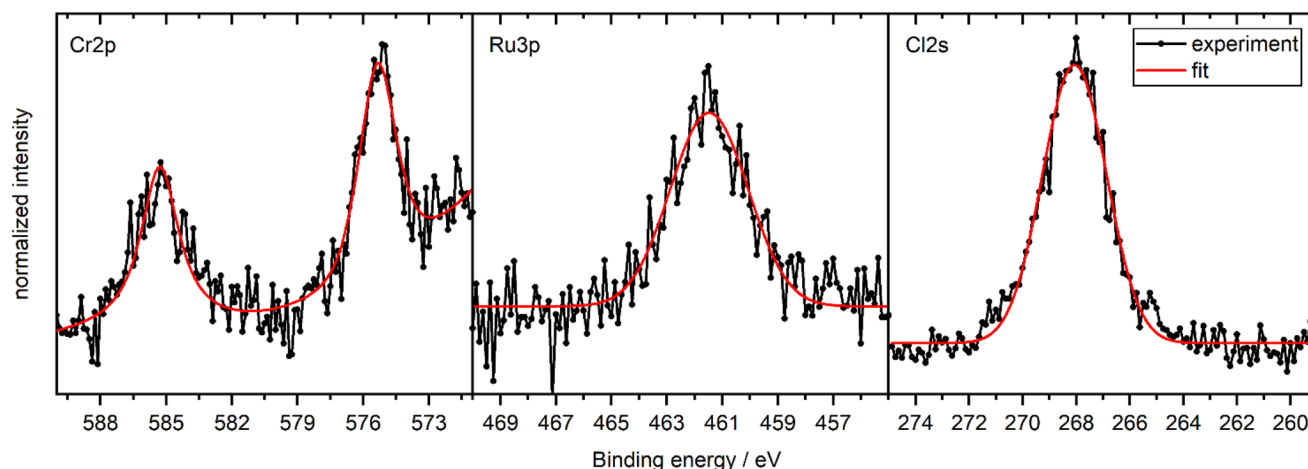


**Fig. 9** Binding energy regions for relevant elements from XPS. All Peaks are assigned to one component, confirming the absence of surface oxidation or other impurities on the surface.
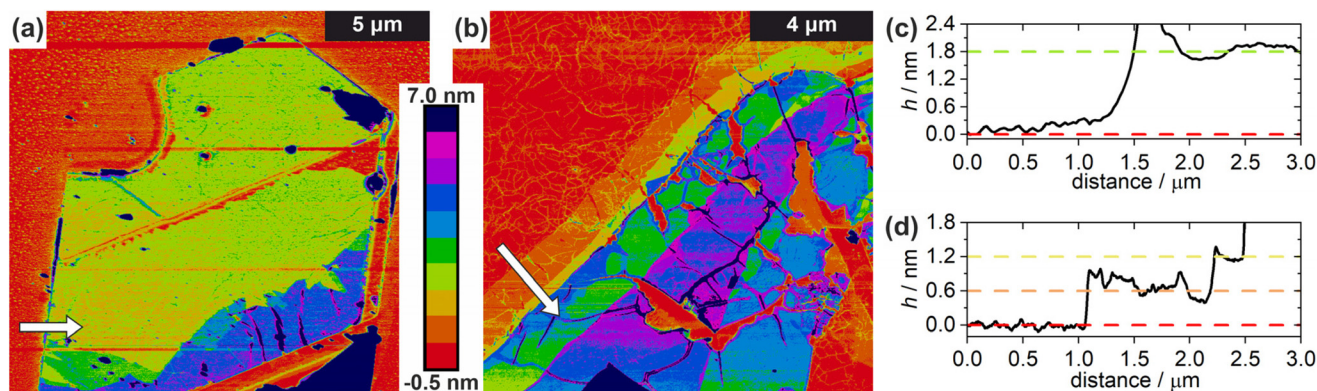
**Fig. 10** AFM measurements of few-layer structures produced by delamination: (a) large area trilayer crystal, (b) structure with stacked mono- and bilayer areas on the edge. (c + d) height profiles of the steps in (a) and (b) marked by the white arrow.

duced with the same starting material of $x = 0.7$ and fits perfect into the trend of enrichment effects over the whole composition range, see Fig. 5(b).

## Delamination of nanocrystals

To reduce the height of the as grown nanocrystals even further and to uncover more nanocrystals on the substrate, an additional delamination by ultrasonication was performed. Because of the relatively weak van der Waals-forces between the layers, ultrasonication can peel off several layers to leave a crystal with a reduced height behind (see ESI Fig. S11†). This can also lead to a shattering of crystals, leaving behind ultrathin structures with stair-like arrangements of layers. In some cases, this results in the uncovering of few- and even monolayer structures, as seen in Fig. 10. As a welcome side effect of such ultrasonic treatment, bigger crystal agglomerates with only small areas of epitaxial growth on the substrate (like in Fig. 6(a)) get removed, which sometimes results in the uncovering of additional nanosheets underneath. This increases the number of nanostructures for further use significantly, even though the delamination process can in some cases decrease the effective area of nanocrystals because of shattering and cracks. Note that the structures below approximately 10 nm are very hard or even impossible to observe with an optical microscope or SEM and need to be identified by AFM investigations. The few-layer structures presented here were always found near or connected to somewhat thicker nanocrystals that are visible with an optical microscope. This delamination technique is therefore suitable to easily produce as-grown few- and monolayer structures directly on the substrate.

confirmed the purity and homogeneity of the solid solution powders. Simulations of the CVT process identified $CrCl_3$ (g), $CrCl_4$ (g), $RuCl_3$ (g) and $RuCl_4$ (g) as the main transport relevant vapour species, as well as $Cl_2$ (g) as an intrinsically generated transport agent formed by marginal decomposition of the mixed crystals. The simulations also predicted an enrichment of chromium chloride during the transport over the whole composition range. We provided experimental results for the composition of the deposited crystals for two different temperature gradients to confirm the chromium chloride enrichment already predicted by the simulations. This enrichment effect must be considered when growing crystals of $Cr_{1-x}Ru_xCl_3$. By choosing advantageous transport parameters, we are able to deposit flat micro- and nanosheets with a predictable composition directly on a YSZ (111) substrate with heights down to about 30 nm and several µm in the lateral size. The characterisations of the deposited nanostructures confirm a high crystallinity quality of the solid solution crystals synthesized by this approach. A delamination of the deposited crystals by an ultrasonic treatment reveals few- and even monolayer structures of the solid solution crystals directly on the substrate without the need for exfoliation. These structures can be of particular interest for detailed studies about the downscaling effects of physical properties, for example magnetic behaviour at low temperatures or catalytic effects. Since CVT of a solid solution is mainly limited by identifying suitable transport parameters at which all components of a mixture are transported simultaneously, this method should be applicable to a large variety of possible 2D solid solutions, also outside the class of TMTHs like transition metal chalcogenides.

## Conclusions

In this study we investigated the synthesis and consecutive chemical vapour transport of $Cr_{1-x}Ru_xCl_3$ solid solution without an external transport agent for the deposition of micro- and nanocrystals. XRD analyses revealed only slight deviations of all unit cell parameters from Vegard's law and

## Author contributions

S. F., P. S. and S. H. designed the research. P. S. and S. H. did fund acquisition. S. F. performed investigation activities, excluding Raman, TEM, XPS and STA measurements. D. W. performed TEM characterisation. M. H. performed XPS characterisation. L. G. and S. F. performed XRD

characterisation. M. W. performed STA characterisation. P. S., S. H., N. G. and B. B. performed project administration and supervision. S. F. wrote the manuscript. All authors reviewed and discussed on the manuscript jointly.

## Conflicts of interest

The authors declare that there are no competing interests.

## Acknowledgements

## References

1 O. Samy, S. Zeng, M. D. Birowosuto and A. El Moutaouakil, *Crystals*, 2021, **11**, 355.

2 A. G.-M. Ferrari, S. J. Rowley-Neale and C. E. Banks, *Anal. Bioanal. Chem.*, 2021, **413**, 663–672.

3 M. Qiu, W. X. Ren, T. Jeong, M. Won, G. Y. Park, D. K. Sang, L. P. Liu, H. Zhang and J. S. Kim, *Chem. Soc. Rev.*, 2018, **47**, 5588–5601.

4 M. A. McGuire, *Crystals*, 2017, **7**, 121.

5 A. Molina-Sánchez, G. Catarina, D. Sangalli and J. Fernández-Rossier, *J. Mater. Chem. C*, 2020, **8**, 8856–8863.

6 D. Weber, L. M. Schoop, V. Duppel, J. M. Lippmann, J. Nuss and B. V. Lotsch, *Nano Lett.*, 2016, **16**, 3578–3584.

7 Y. Wang, Y. Jin, L. Wang, Z. Hao, C. Liu, Y. J. Hao, X. M. Ma, S. Kumar, E. F. Schwier, K. Shimada, C. Liu, J. Mei, H. Xu and C. Chen, *Phys. Rev. B*, 2021, **103**, 035150.

8 H. Hillebrecht, P. J. Schmidt, H. W. Rotter, G. Thiele, P. Zönnchen, H. Bengel, H. J. Cantow, S. N. Magonov and M. H. Whangbo, *J. Alloys Compd.*, 1997, **246**, 70–79.

9 G. Bastien, M. Roslova, M. H. Haghighi, K. Mehlawat, J. Hunger, A. Isaeva, T. Doert, M. Vojta, B. Büchner and A. U. B. Wolter, *Phys. Rev. B*, 2019, **99**, 214410.

10 Y.-J. Yuan, C.-H. Li, S.-J. Tian, H.-C. Lei and X. Zhang, *Chin. Phys. Lett.*, 2020, **37**, 067501.

11 T. Klaproth, E. Müller, C. Habenicht, B. Büchner, M. Knupfer, M. Roslova, A. Isaeva, T. Doert and A. Koitzsch, *Phys. Rev. Mater.*, 2022, **6**, 014001.

12 D. R. Klein, D. MacNeill, Q. Song, D. T. Larson, S. Fang, M. Xu, R. A. Ribeiro, P. C. Canfield, E. Kaxiras, R. Comin and P. Jarillo-Herrero, *Nat. Phys.*, 2019, **15**, 1255–1260.

13 H. H. Kim, B. Yang, S. Li, S. Jiang, C. Jin, Z. Tao, G. Nichols, F. Sfigakis, S. Zhong, C. Li, S. Tian, D. G. Cory, G. X. Miao, J. Shan, K. F. Mak, H. Lei, K. Sun, L. Zhao and A. W. Tsen, *Proc. Natl. Acad. Sci. U. S. A.*, 2019, **166**, 11131–11136.

14 B. Zhou, Y. Wang, G. B. Osterhoudt, P. Lampen-Kelley, D. Mandrus, R. He, K. S. Burch and E. A. Henriksen, *J. Phys. Chem. Solids*, 2019, **128**, 291–295.

15 D. Weber, L. M. Schoop, V. Duppel, J. M. Lippmann, J. Nuss and B. V. Lotsch, *Nano Lett.*, 2016, **16**, 3578–3584.

16 F. Hansen, M. Wels, S. Froeschke, A. Popov, D. Wolf, B. Büchner, P. Schmidt and S. Hampel, *Cryst. Growth Des.*, 2020, **20**, 7341–7349.

17 D. Hu, G. Xu, L. Xing, X. Yan, J. Wang, J. Zheng, Z. Lu, P. Wang, X. Pan and L. Jiao, *Angew. Chem., Int. Ed.*, 2017, **56**, 3611–3615.

18 M. Grönke, D. Pohflepp, P. Schmidt, M. Valldor, S. Oswald, D. Wolf, Q. Hao, U. Steiner, B. Büchner and S. Hampel, *Nano-Struct. Nano-Objects*, 2019, **19**, 100324.

19 U. Hotje, R. Wartchow and M. Binnewies, *Z. Naturforsch., B: Chem. Sci.*, 2005, **60**, 1235–1240.

20 G. Krabbes, J. Klosowski, H. Oppermann and H. Mai, *Cryst. Res. Technol.*, 1984, **19**, 491–498.

21 B. H. Toby and R. B. Von Dreele, *J. Appl. Crystallogr.*, 2013, **46**, 544–549.

22 B. Morosin and A. Narath, *J. Chem. Phys.*, 1964, **40**, 1958–1967.

23 R. D. Johnson, S. C. Williams, A. A. Haghighirad, J. Singleton, V. Zapf, P. Manuel, I. I. Mazin, Y. Li, H. O. Jeschke, R. Valentí and R. Coldea, *Phys. Rev. B: Condens. Matter Mater. Phys.*, 2015, **92**, 235119.

24 G. Krabbes, W. Bieger, K.-H. Sommer, T. Söhnel and U. Steiner, *TRAGMIN 5.1*, Dresden, 2014.

25 M. Roslova, J. Hunger, G. Bastien, D. Pohl, H. M. Haghighi, A. U. B. Wolter, A. Isaeva, U. Schwarz, B. Rellinghaus, K. Nielsch, B. Büchner and T. Doert, *Inorg. Chem.*, 2019, **58**, 6659–6668.

26 M. A. McGuire, J. Yan, P. Lampen-Kelley, A. F. May, V. R. Cooper, L. Lindsay, A. Puretzky, L. Liang, S. Kc, E. Cakmak, S. Calder and B. C. Sales, *Phys. Rev. Mater.*, 2017, **1**, 064001.

27 M. Binnewies, R. Glaum, M. Schmidt and P. Schmidt, *Chemical Vapor Transport Reactions*, De Gruyter, Berlin/Boston, 2012.

28 M. Grönke, P. Schmidt, M. Valldor, S. Oswald, D. Wolf, A. Lubk, B. Büchner and S. Hampel, *Nanoscale*, 2018, **10**, 19014–19022.

29 M. Grönke, B. Buschbeck, P. Schmidt, M. Valldor, S. Oswald, Q. Hao, A. Lubk, D. Wolf, U. Steiner, B. Büchner and S. Hampel, *Adv. Mater. Interfaces*, 2019, **6**, 1901410.

30 Z.-P. Cheng, B. G. He, H. Li and W. B. Zhang, *J. Phys.: Condens. Matter*, 2021, **33**, 355401.

31 T. T. Mai, A. McCreary, P. Lampen-Kelley, N. Butch, J. R. Simpson, J. Q. Yan, S. E. Nagler, D. Mandrus, A. R. H. Walker and R. V. Aguilar, *Phys. Rev. B*, 2019, **100**, 134419.